batteries

MDPI

Article

Melamine-Sacrificed Pyrolytic Synthesis of Spiderweb-like Nanocages Encapsulated with Catalytic Co Atoms as Cathode for Advanced Li-S Batteries

Han Wang [1,2], Sidra Jamil [1,2], Wenwen Tang [1,2], Jing Zhao [1,2], Hui Liu [1,2], Shujuan Bao [1,2], Yijun Liu [1,2,*] and Maowen Xu [1,2,*]

[1] Key Laboratory of Luminescent and Real-Time Analytical Chemistry (Southwest University), Ministry of Education, Institute of Materials and Energy, Southwest University, Chongqing 400715, China
[2] Chongqing Key Lab for Advanced Materials and Clean Energies of Technologies, School of Materials and Energy, Southwest University, Chongqing 400715, China
* Correspondence: liuyj26@swu.edu.cn (Y.L.); xumaowen@swu.edu.cn (M.X.)

Abstract: Due to the high theoretical capacity of 1675 mAh g^{-1} of sulfur, lithium-sulfur (Li-S) batteries can reach a high energy density of 2600 Wh kg^{-1}, which has shown fascinating potential in recent decades. Herein, we report the spiderweb-like nanocage (Co/Mel) as a novel sulfur host with a melamine-sacrificed pyrolysis method. The incorporation of embedded cobalt nanoparticles (Co NPs) in the tips of carbon nanotubes (CNTs) can catalyze polysulfide transformation kinetics. In addition, the nanocages form a conductive three-dimensional spiderweb-like network that facilitates electrolytic penetration and electronic/ionic transportation. Moreover, the porous internal nanocavities not only improve sulfur loading levels but also provide buffer space for volume expansion during charging and discharging. As a result, the hollow Co/Mel polyhedra with a high content of sulfur (75.5 wt%) displays outstanding electrochemical performance with an initial discharge-specific capacity of 1425.2 mAh g^{-1} at 0.1 C and a low decay rate of only 0.028% after 1000 cycles at 1 C.

Keywords: lithium-sulfur batteries; pyrolytic synthesis; zeolite imidazolate framework; spiderweb-like nanocages; catalytic conversion

Citation: Wang, H.; Jamil, S.; Tang, W.; Zhao, J.; Liu, H.; Bao, S.; Liu, Y.; Xu, M. Melamine-Sacrificed Pyrolytic Synthesis of Spiderweb-like Nanocages Encapsulated with Catalytic Co Atoms as Cathode for Advanced Li-S Batteries. *Batteries* **2022**, *8*, 161. https://doi.org/10.3390/batteries8100161

Academic Editor: Carlos Ziebert

Received: 31 August 2022
Accepted: 1 October 2022
Published: 6 October 2022

1. Introduction

Although traditional fossil fuels have made enormous contributions to the improvement of human life, increasing fossil fuel consumption has resulted in a series of knock-on effects on Earth, such as global warming and the greenhouse effect [1–4]. Hence, we need to develop cleaner energy conversion and storage systems. Li-S batteries have proven to be one of the best candidates for next-generation energy storage devices because of their high energy density, which exceeds that of conventional lithium-ion batteries [5–7]. However, with the deeper study of Li-S batteries, several challenges regarding the sulfur electrode have emerged, including the slow deposition kinetics of lithium polysulfides (LiPSs) at low electrolyte/sulfur (E/S) ratios, which leads to low coulombic efficiency, the collapse of the electrode structure, capacity degradation due to the continuous expansion/contraction during charge and discharge, the insulating nature of the sulfur substance and low active material utilization [8–13]. Therefore, these complex issues must be addressed in order to achieve practical applications. As a consequence, the design of electrode material structure is paramount.

Metal-organic frameworks (MOFs) are a new class of polymeric material with a periodic porous network structure formed by self-assembly through an organic-inorganic hybrid [14], with different geographies, topologies and functions leading to tunable chemophysical characteristics based on the type and connectivity of the two parts [15,16]. In the past few decades, with the growing interest in nanometer-scale confined domains,

hundreds of MOFs have been obtained and studied every year [17–19]. Although there are some reported applications in energy storage systems, Li-S batteries involve the complicated transport and reaction of electroactive components of different sizes and charged states [20–23]. The regulation of these processes raises different requirements on material design in terms of pore structure, pore environment, the abundance of MOF inorganic nodes and designable organic linkers which allow a tailored micro-structure enabling tunable interactions with the electroactive components in Li-S batteries [24]. Thus, it is crucial to investigate the structure-effect relationship when synthesizing MOF-derived materials as sulfur hosts for Li-S batteries.

A lot of research has been dedicated to the use of MOFs as templates for immobilizing sulfur. For example, Zhang's group [25] used a self-template method to synthesize MOF-derived CoP-HNC nanocages. Jeon and co-workers [26] fabricated the core/shell structure of Zn/Co bimetallic MOF/ZnO nanospheres. Xie et al. [27] constructed MOF-derived bifunctional $Co_{0.85}Se$ nanoparticles embedded in carbon nanosheet arrays. MOF-derived materials not only possess the porous structure of the MOF, but also expose rich metal nodes to act as active sites, rendering strong LiPS absorbability. Therefore, these MOF-derived materials can achieve a low capacity-fading rate over long-term cycling based on their structural advantages when applied as sulfur hosts for Li-S batteries.

Accordingly, in this work, we fabricated a porous 3D network cross-linked hollow structure which mimics spiderweb based on a ZIF-67 precursor with a simple melamine-sacrificed pyrolysis method. As shown in Figure 1, ZIF-67 was a simple template for the construction of a hollow 3D Co/Mel electrode which was endowed with catalytic sites for LiPS capture, while the CNTs network grown in situ on the surface of ZIF-67 enhanced the conductivity. Through these synergistic virtues, the shuttle effect of polysulfides can be effectively suppressed. Additionally, the conductive skeleton with a large specific surface area can also alleviate volume expansion and improve the utilization of the active substance to achieve a significantly high specific capacity and stable cycle life when used as host materials for sulfur.

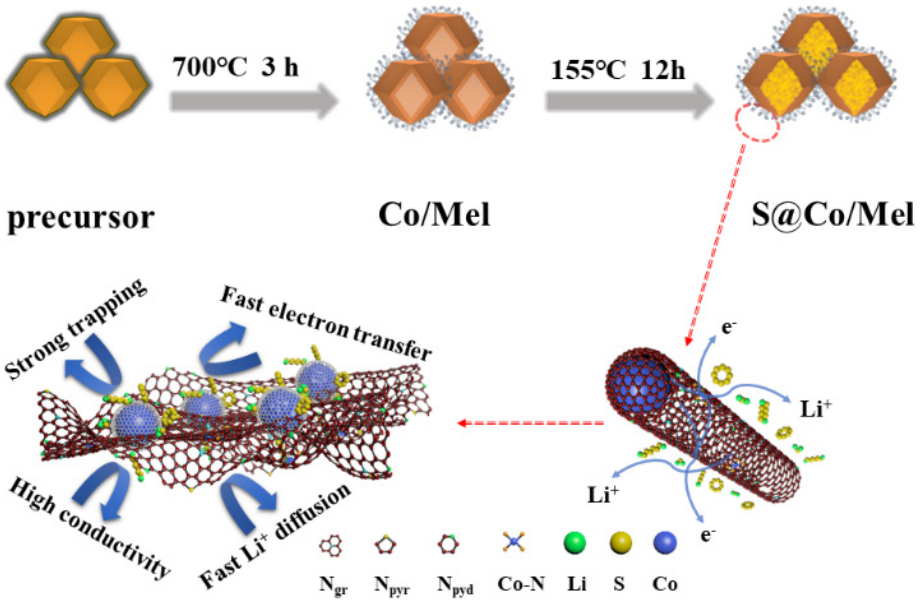

Figure 1. Schematic illustration of the synthesis and structure of S@Co/Mel composite.

2. Materials and Methods

2.1. Materials

Cobalt nitrate hexahydrate ($Co(NO_3)_2 \cdot 6H_2O$, >99%), 2-methylimidazole (2-MI, >98%), melamine (99%) and sublimed sulfur (>99.5%) were purchased from Aladdin (Shanghai, China) without further purification.

2.2. Synthesis of ZIF-67

In a typical process, 1.16 g $Co(NO_3)_2 \cdot 6H_2O$ (4 mmol) and 1.31 g 2-MI (16 mmol) were dissolved in 200 mL methanol, respectively. Then the 2-MI solution was quickly poured into the $Co(NO_3)_2$ solution to form a homogeneous solution under vigorous stirring for 24 h at room temperature. The purple precipitate was collected via centrifugation and washing with methanol three times and then dried at 60 °C for 12 h in a vacuum oven to remove the solvent.

2.3. Synthesis of Co/Mel

A total of 0.1 g ZIF-67 precursor and 0.1 g melamine were dispersed into 100 mL methanol under ultrasound for 2 h. The precipitate was collected by vacuum filtration, washed with methanol three times and then dried at 60 °C for 12 h. The mixture was then transferred into a tube furnace and annealed under Ar flow at 700 °C for 3 h with a heating rate of 2 °C min^{-1} to obtain the Co/Mel product. As a reference sample, a product named Co/NC was made under the same conditions with only ZIF-67 as precursor.

2.4. Synthesis of S@Co/Mel

A sulfur cathode was prepared through molten diffusion. Typically, 0.4 g sulfur and 0.1 g as-collected Co/Mel sample were ground into a fine powder for 30 min. Then, the hybrid was annealed at 155 °C for 12 h in Ar atmosphere with a heating rate of 2 °C min^{-1}. Afterwards, the S@Co/Mel composite was obtained. For a fair comparison, the S@Co/NC product was prepared in the same way.

2.5. Adsorption Experiment

The 0.2 M Li_2S_6 solution was synthesized by mixing sulfur and lithium sulfide together at a molar ratio of 5:1 in a mixture of 1,2-dimethoxyethane (DME) and 1,3-dioxolane (DOL) (v/v = 1:1), followed by vigorous stirring for two days inside an argon-filled glove box at room temperature. A total of 10 mg each of Co/Mel and Co/NC were added into the as-prepared Li_2S_6 solution, with the blank Li_2S_6 solution as a reference. The different adsorbents in sealed vials were kept standing for 12 h, and then the supernatants were used for the UV-vis test.

2.6. Li_2S Deposition

To prepare the Li_2S_8 solution (0.2 M), the mixture of Li_2S and sulfur with a mass ratio of 1:7 was added into DOL and DME (1:1, v/v) and then stirred at 60 °C for 48 h in Ar atmosphere. In this experiment, we used carbon fiber paper to load Co/Mel as the working electrode, Li foil as the counter electrode and Celgard 2400 membrane as the separator. A total of 20 μL of Li_2S_8 catholyte was added onto the working electrode, while 20 μL of blank electrolyte, without Li_2S_8 but otherwise identical, was added onto the counter electrode. The fabricated cell was galvanostatically discharged to 2.06 V at 0.112 mA, followed by discharging potentiostatically at 2.05 V.

2.7. Electrochemical Measurement

The final S@Co/Mel product was mixed with acetylene black (AB) and polyvinylidene fluoride (PVDF) at a mass ratio of 8:1:1, and afterwards dropped in N-methyl-2-pyrrolidone (NMP) with fierce grinding, and then coated on Al foil using a doctor blade and dried at 60 °C in an oven; the average mass loading of the active material was 1.0 mg cm^{-2}. The coin-type batteries (CR2032) were assembled in Ar atmosphere, with Li metal as counter electrode and Celgard 2400 polypropylene membrane as separator. The electrolyte was 1.0 M lithium bis (trifluoromethanesulfonyl) sulfonamide (LiTFSI) salt dissolved in DME and DOL (1:1 by volume) with $LiNO_3$ (1 wt%) as additive. After standing for 12 h to guarantee the full infiltration, galvanostatic charge/discharge tests were carried out by the Land testing system (Wuhan Kingnuo Electronic Co., Wuhan, China) within a potential range of 1.7–2.8 V (vs. Li/Li^+). The cyclic voltammetry (CV) curves were collected with

CHI 660E electrochemical workstation (Shanghai Chenhua Instruments, China) at a scan rate of 0.1 mV s^{-1} in the voltage window of 1.7–2.8 V. The electrochemical impedance spectroscopy (EIS) was tested with a Zahner electrochemical workstation at the open circuit potential (OCP) with a frequency between 100 kHz and 0.01 Hz.

2.8. Physical Characterization

The morphology and internal structure of the synthesized samples were characterized by field emission scanning electron microscopy (FESEM, JSM-7800F, Tokyo, Japan) and transmission electron microscopy (TEM, JEM-2100, Tokyo, Japan). The composition of the material was investigated by energy dispersive spectroscopy (EDS, JEOL6300F, Tokyo, Japan). The crystal structure of the powder was analyzed by X-ray diffraction (XRD, MAXima-X XRD-7000) with Cu Kα radiation (λ = 1.5406 Å) in the range of 10–80°. Raman spectra were conducted at 532 nm laser wavelength (Raman, LabRAM HR Evolution, Horiba, France). The surface chemical properties of the materials were detected by X-ray photoelectron spectroscopy (XPS, ESCALAB 250Xi, Waltham, MA, USA). The sulfur content of the cathode was examined by a thermogravimetric analyzer (TGA, Q50, New Castle, DE, USA) at a heating rate of 10 °C min^{-1} under N_2 atmosphere. The specific surface area and pore size distribution were determined by Quantachrome instrument (BET, Quadrasorb evo 2QDS-MP-30, Boynton Beach, FL, USA).

2.9. In Situ Test

In situ XRD analysis was performed with equipment from Bruker (Beijing) Technology Co., LTD. The cathode was prepared by coating the slurry onto an aluminum foil, and the potential range of 1.7–2.8 V was set at a C/10 rate with a Land battery testing system. In situ Raman analysis was obtained by setting a CV program on CHI760E using EL-Cell, Germany. Lab-RAM HR Evolution (Horiba) with an excitation laser wavelength of 532 nm was utilized to test and simultaneously recorded the reading after every 15 min interval.

3. Discussion

The S@Co/Mel compound of nitrogen-doped CNTs was synthesized in situ on the ZIF-67 surface using feasible melamine-sacrificed pyrolysis and melt-diffusion strategy, as schematically depicted in Figure 1. After calcining the melamine-encapsulating precursor at 700 °C, the as-formed Co@Mel became very rough and a layer of furry nanowires could be seen on its surface, similar to a spiderweb. After 12 h sulfur loading, the structure of the nanocavity was able to contain the sulfur very well.

The ZIF-67 precursor was obtained with a homogeneous smooth dodecahedral morphology (Figure 2a,d) and a size distribution of approximately 600 nm, as shown in the field-emission scanning electron microscopy (FESEM) photographs. After calcination with melamine, a polycondensation reaction occurs as the temperature gradually increases from room temperature, releasing several reactive cyano species such as $C_3N_2^+$ and CN_2^+ [28,29]. Accompanied by the decomposition of melamine, the network of rough nitrogen-doped CNTs encapsulated with Co NPs was grown in situ on the surface of ZIF-67 (Figure 2c) at 700 °C, which resulted in the final spiderweb-like nanocages. For the post-pyrolysis product, the yolk-shell structure of Co/Mel is easily distinguishable in Figure 2f. Meanwhile, its morphology does not collapse after calcination. Notably, the Co/Mel matrix retains its typical dodecahedral structure, indicating that the material has thermal stability and can withstand the stress changes caused by temperature variations. In contrast, when synthesized without melamine, CNTs were negligible on the surface of the final product (Figure 2b,e).

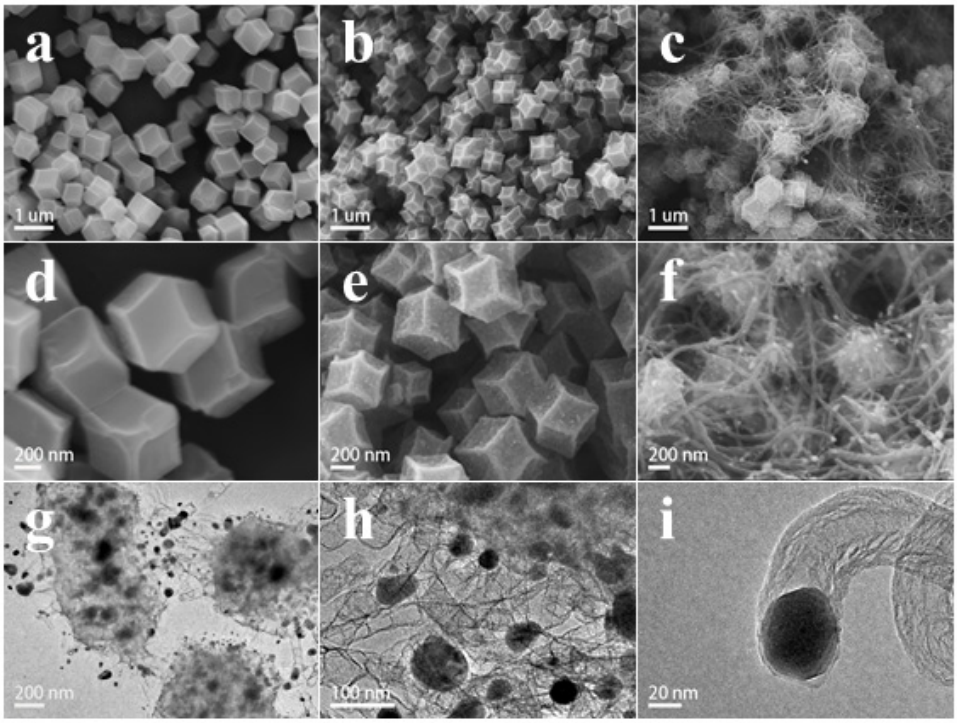

Figure 2. SEM images of ZIF-67 (**a**), Co/NC (**b**) and Co/Mel (**c**); FESEM images of ZIF-67 (**d**), Co/NC (**e**) and Co/Mel (**f**); HRTEM images of Co/Mel (**g**–**i**).

The TEM images in Figure 2g clearly indicate that the material exhibits a prominent porous structure, with the black dots corresponding to Co NPs evenly embedded within the carbon matrix. Figure 2h,i reveals the uniform distribution of dodecahedral ZIF-67 entangled with CNTs, the tiny Co NPs were encapsulated in the tips of the CNTs and an interlayer distance of 0.20 nm was determined, corresponding to the Co (111) lattice plane (JCPDS #15-0806). The HRTEM images confirm that the thick multi-walled carbon nanotubes (MWCNTs) with a d-spacing of 0.34 nm reflected in the (002) lattice plane are perfectly parallel [30], suggesting the presence of graphitic layers (Figure 3a). The two transparent lattice diffraction fringes can be identified, one at 1.7723 Å and the other at 2.0467 Å [31], attributed to the (200) and (111) lattice planes of Co, as shown in Figure 3b. Meanwhile, selected area electron diffraction (SAED in Figure 3c) also indicates that the polycrystalline diffraction rings are well-matched with the cubic cobalt. C, N and Co were detected in EDS spectra and mapping, illustrated in Figure 3d and Figure S1.

The X-ray diffraction (XRD) pattern of ZIF-67 is displayed in Figure S2a, showing the sharp diffraction peak at 7.2° which indicates that the ZIF-67 precursor has excellent crystallinity [32]. Figure 3e illustrates the XRD patterns of Co/Mel, with most of the diffraction peaks of ZIF-67 disappearing after the high-temperature annealing treatment while replaced by three characteristic peaks of cubic cobalt (JCPDS#15-0806) with a larger half-peak width [33]. This phenomenon suggests that the one-step melamine-sacrificed pyrolysis route can promote the conversion of Co^{2+} into highly dispersed and nano-sized cobalt particles. Furthermore, the wider diffraction peak at 26.4/26.1° corresponds to partially graphitized carbon [34], confirming that the presence of Co NPs contributes to the conversion of amorphous carbon to graphitized carbon [35]. The characteristic peaks of cobalt with low intensity can still be observed in Co/NC (Figure S2b). The specific surface area and pore size distribution of Co/Mel were evaluated by Brunauer-Emmett-Teller (BET), and Barrett-Joyner-Halenda (BJH) theory at 77 K [36]. The Co/Mel nitrogen adsorption–desorption isotherm has the characteristics of a IV-type hysteresis loop in Figure 3f with the specific surface area of 249.22 m^2 g^{-1}. Furthermore, a relatively narrow

mesopore size distribution can be found in the pore volume vs. pore size distribution curve. It has an average pore size of 4 nm and a pore volume of 0.643 cm^3 g^{-1}.

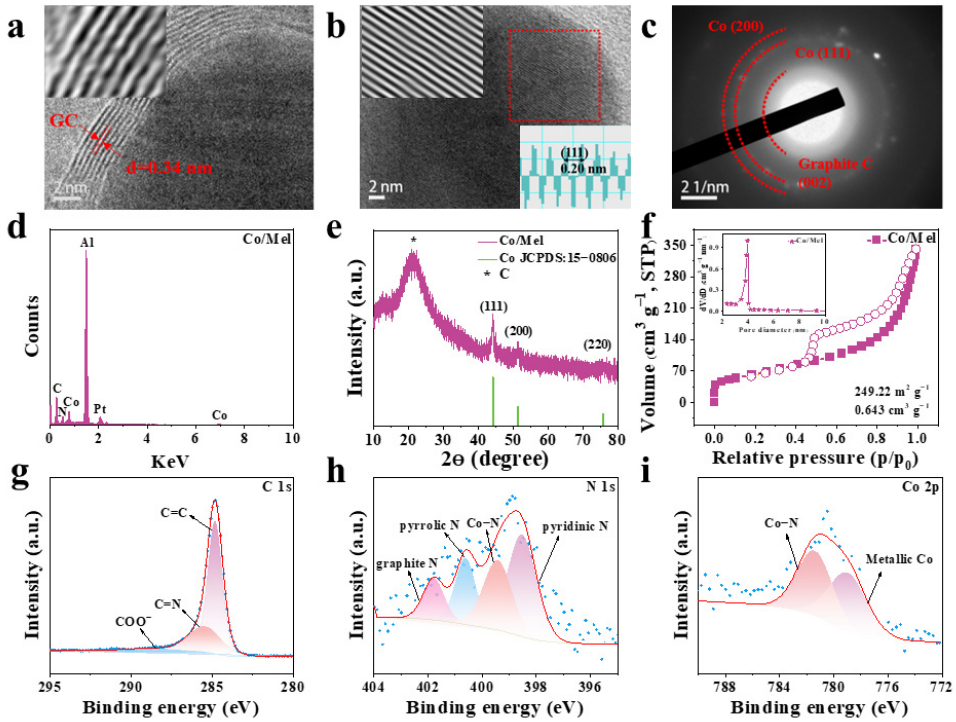

Figure 3. HRTEM images of Co/Mel (**a**,**b**); SAED image of Co/Mel (**c**); EDS spectra of Co/Mel (**d**); XRD pattern of Co/Mel (**e**); N_2 adsorption-desorption isotherm and pore size distribution curve of Co/Mel (**f**); XPS spectra of C 1s (**g**), N 1s (**h**) and Co 2p (**i**) of Co/Mel.

X-ray photoelectron spectroscopy (XPS) was performed on Co/Mel to investigate the internal chemical bonds and valence states [37]. The high-resolution XPS spectra of carbon (C 1s), nitrogen (N 1s) and cobalt (Co 2p) are shown in Figure 3g–i. The deconvoluted XPS spectrum of C 1s (Figure 3g) has major peaks at 284.5 eV, 285.5 eV and 287.8 eV, attributed to typical C=C, C=N and COO^-, respectively. The high-resolution spectra of N (Figure 3h) are due to spin-orbit coupling that can be deconvoluted into four sub-peaks, including pyridine-N (398.5 eV), Co-N (399.43 eV), pyrrole-N (400.6 eV) and graphite-N (401.8 eV), respectively. The existence of the Co-N not only provides strong bind sites for lithium polysulfide by means of chemical affinity but also improves the uniform distribution of Co NPs in the carbon matrix. The deconvoluted XPS spectrum of Co 2p (Figure 3i) presents two chemically distinct peaks. The peak at 778.2 eV is metallic Co and the peak at 781 eV may be mainly contributed by the Co-N bonds. Moreover, Co-N bonds are believed to play vital roles in facilitating the electrocatalytic process [38].

Finally, the S@Co/Mel cathode material was prepared in a simple melt-diffusion approach of commercial sulfur into the synergistic controlled pore structure. No large bulk of sublimed sulfur is observed in Figure 4a,b, indicating that the pore structure is filled mainly with sulfur. The energy-dispersive X-ray spectroscopy (EDS) mapping images (Figure 4c) display the uniform dispersion of C/N/Co/S elements, further explaining that sulfur is injected into the hollow polyhedron. Moreover, the co-existence of common elements (C, N) and cobalt confirms the in situ doping in porous carbon material as well as the homogeneous dispersion of Co NPs in the carbon matrix.

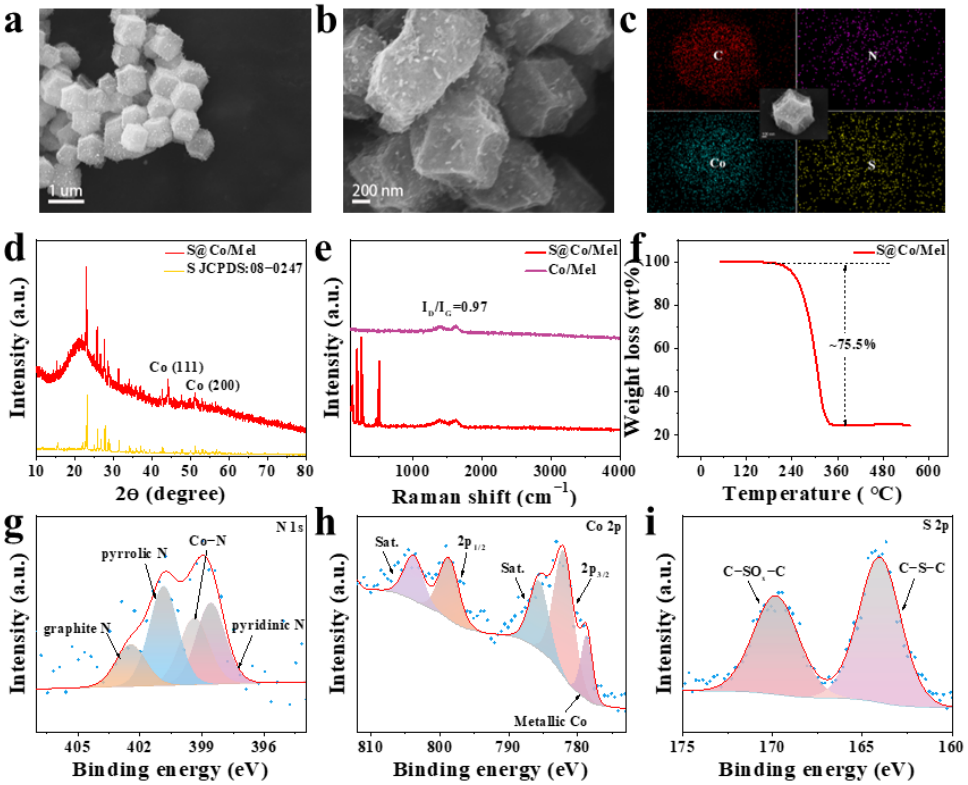

Figure 4. FESEM images of S@Co/Mel (**a**,**b**); EDS spectra of S@Co/Mel (**c**); XRD pattern of S@Co/Mel and S (**d**); Raman spectra of Co/Mel and S@Co/Mel (**e**); TGA curve of S@Co/Mel in the N_2 atmosphere (**f**); XPS spectra of N 1s (**g**), Co 2p (**h**) and S 2p (**i**) of S@Co/Mel.

The diffraction pattern of the composite S@Co/Mel shows a sulfur peak on a carbon background (Figure 4d), which corresponds well to the characteristic peak of sublimed sulfur, indicating that S has been successfully composited with porous carbon materials. Raman measurements have been carried out to investigate the structural properties of the synthesized samples, showing two specific D and G bands at 1381 and 1594 cm^{-1}, respectively, consistent with the presence of graphitic carbon observed in the HRTEM images. The appearance of the G-band is attributed to in-plane vibrations of the sp^2-hybridized graphitized structure, while the D-band provides evidence for the presence of sp^3-hybridized disordered structure [39]. The degree of disorder or graphitization of carbon materials is judged by the intensity ratio of the D-band to the G-band. Co/NC shows an I_D/I_G ratio of 1.06 (Figure S2d); whereas, after melamine-sacrificed pyrolysis treatment, the I_D/I_G ratio decreases to 0.97, indicating that the material has both graphitic and disordered structures, but the degree of graphitization is higher [40]. When sulfur is loaded, the specific peak of S can be observed at 192 cm^{-1} and 504 cm^{-1} in the Raman spectrum of S@Co/Mel (Figure 4e). The sulfur content of the composite was analyzed using a Thermogravimetric analysis (TGA) method. As shown in Figure 4f, the curve starts to exhibit weight loss due to the sublimation of sulfur at around 155 °C, eventually revealing a sulfur content of 75.5% in the composite. This sulfur-loading process also leads to a distinct reduction in surface area and pore volume, which correspond to 24.19 m^2 g^{-1} and 0.047 cm^3 g^{-1}, respectively. This further illustrates the successful encapsulation of sublimed sulfur and its limitation by mesoporosity, as shown in Figure S3a,b. Additionally, it is worth noting that the specific surface area of the ZIF-67 precursor calcined alone is significantly lower than that of the melamine-containing cobalt material in Figure S3c,d, suggesting that melamine can be used not only as a nitrogen source to generate nitrogen-doped carbon, but also as a pore-forming agent to generate more voids and thus store higher amount of sulfur content as well as shield the volume expansion of sulfur. Furthermore, the increased specific surface area

of the CNTs is widely believed to facilitate electrolyte penetration and ion transportation. More significantly, the ends of the CNTs are inlaid with small Co NPs, exposing more active sites that can enhance the electrochemical activity during the redox reaction of lithium polysulfide. Figure 4g–i shows the XPS survey spectrum of S@Co/Mel, which further verifies the presence of N, Co and S elements in this hybrid composition [41].

Consequently, the host of S@Co/Mel is considered as a good candidate for the sulfur cathode, and the superiority of the S@Co/Mel cathode was verified by assembling Li-S coin cells for the following electrochemical measurements. Figure 5a shows a cyclic voltammetry (CV) test of the electrode assembled with S@Co/Mel composite cathode material to elucidate its electrochemical behavior during the charge/discharge process. The scan rate is 0.1 mv s^{-1} and the voltage range is 1.7–2.8 V (vs Li/Li^+). During the first scan, it can be observed that the curve is basically consistent with the typical CV curve of elemental sulfur, indicating a two-step reduction of sulfur. The sharp reduction peak near 2.25 V corresponds to the reduction of octasulfur (S_8) to soluble higher-order long-chain lithium polysulfide (Li_2S_n, $4 \leq n \leq 8$), while another well-defined reduction peak near 2.02 V corresponds to the further reduction of the long-chain lithium polysulfide to the insoluble Li_2S_2 and Li_2S. As for the subsequent oxidation process, only one broad peak emerges at around 2.40 V, which is associated with a reverse transition of lithium polysulfide back to octasulfur [42–44]. The almost perfect overlap of the CV curves from the second scan is strong evidence for improved reversibility, which indicates a lower degree of irreversible sulfur loss from the shuttle effect and high utilization of the active material during charge and discharge. Significantly, the CV curve of the S@Co/Mel composite presents a weaker polarization reaction compared to the S@Co/NC electrode, which is evidenced by the higher intensity in the anode and cathode peak (Figure S4a).

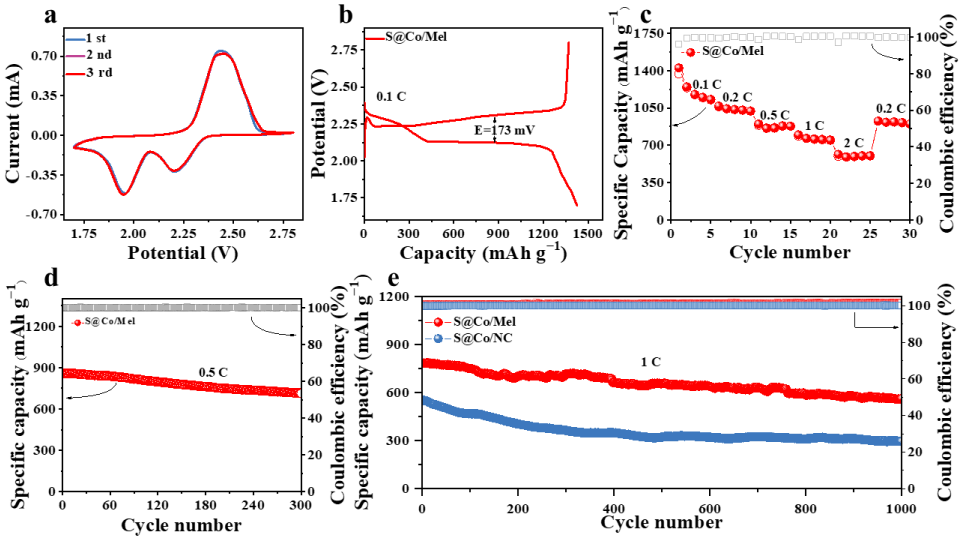

Figure 5. CV curves of S@Co/Mel for three initial cycles at the scan rate of 0.1 mV s^{-1} (**a**); corresponding charge/discharge curve at 0.1 C (**b**); specific capacity at different C rates (**c**); cycling performance at 0.5 C (**d**) and 1 C (**e**) between 1.7–2.8 V.

A galvanostatic discharge-charge behavior with a constant current density of 0.1 C (1 C = 1675 mA g^{-1}) is revealed in Figure 5b, with the range of voltage from 1.7 V to 2.8 V (vs Li/Li^+). Obviously, the curve contains two discharging plateaus; the plateau around 2.25 V corresponds to the first reduction peak of the CV curve, reflecting the transition from S to high-order lithium polysulfide. Correspondingly, the long plateau corresponds to the second reduction peak of the CV curve, revealing the deposition of low-order lithium polysulfide. On the other hand, one typical charging plateau at about 2.3 V corresponds to the transformation from Li_2S_2/Li_2S to octasulfur. Notably, the S@Co/Mel electrode delivers high initial specific capacity values of 1369.7 mAh g^{-1} at 0.1 C. The potential difference

between the two long plateaus is measured as 173 mV and 235 mV for the S@Co/Mel and S@Co/NC cathodes, respectively [45], which indicates that the S@Co/Mel cathode possesses a lower overpotential and a smaller cell polarization by facilitating the redox reaction kinetics (Figure S4b).

The rate performance of the S@Co/Mel cathode at different current densities (from 0.1 C to 2 C) is depicted in Figure 5c. It delivers average specific capacities of 1425.2, 1068.7, 900.0, 798.0 and 614.9 mAh g^{-1} at current rates of 0.1 C, 0.2 C, 0.5 C, 1.0 C and 2.0 C, respectively. When the current density is restored back to 0.2 C, the specific capacity can reach 927.5 mAh g^{-1}, demonstrating good structural stability under high current rates. However, the rate performance of S@Co/NC cathode was inferior in Figure S4c.

The cycling performance of the S@Co/Mel cathode has been evaluated at 0.5 C, as presented in Figure 5d, exhibiting a remarkable initial discharge capacity at 861.7 mAh g^{-1} and retaining a high reversible capacity of 713.6 mAh g^{-1} after 300 cycles, corresponding to a capacity retention of 82.81%, which proves that the electrode structure demonstrates a good sulfur binding effect and helps in the confinement of polysulfide. Comparatively, the contrast sample (S@Co/NC) delivers a lower initial capacity of 763.3 mAh g^{-1} and preserves only 570.3 mAh g^{-1} of reversible capacity after 300 cycles (Figure S4d), thus underlining the outstanding role of our as-synthesized material in terms of excellent electrochemical performance during the whole discharge/charge process. For comparison, the cycling performance at 1 C for S@Co/Mel and S@Co/NC is shown in Figure 5e. Remarkably, S@Co/Mel delivers an initial discharge capacity of 781.9 mAh g^{-1} higher than that of S@Co/NC (553.1 mAh g^{-1}). After the long-term cycling for 1000 cycles, S@Co/Mel retained 563 mAh g^{-1}, but S@Co/NC only retains 295.9 Amh g^{-1}, corresponding to a capacity decay of 0.028% and 0.047%, respectively. Exceptionally, the coulombic efficiency of S@Co/Mel is almost 100% throughout the long-term cycling.

To better understand the catalytic process and strong chemisorption towards lithium polysulfides, the Li_2S deposition and ultraviolet–visible spectroscopy (UV-vis) measurement are conducted. As demonstrated in Figure 6a and Figure S5, the smooth trapping–diffusion–conversion of LiPSs ensures the high electrochemical performance of Co/Mel, which illustrates that the design of the 3D conductive network can guarantee faster electron transport and a uniform deposition process during charging/discharging. The electrochemical impedance spectroscopy (EIS) of the S@Co/Mel and S@Co/NC batteries at OCP were carried out in Figure 6b. According to previous studies [46], the semicircle diameter in the high-frequency region indicates the charge transfer resistance (R_{ct}), while the slope of the oblique line in the low-frequency region represents the ion diffusion resistance (R_{id}). Figure 6b illustrates that the R_{ct} value of S@Co/Mel is much smaller than that of S@Co/NC, confirming that introducing Co NPs into the three-dimensional spiderweb-like network structure reduces the resistance of charge transfer due to its catalytic activity and superior conductivity [47].

In order to better understand the complete reaction process, in situ experiments are necessary. As shown in the in situ Raman spectroscopy in Figure 6c, some typical signals of S_8 at 188.5 cm^{-1}, 255.2 cm^{-1} and 508.2 cm^{-1} are observed at open circuit potential (OCP). As the discharge goes on, the peaks at 430.8 cm^{-1} and 481.3 cm^{-1} emerge, revealing the formation of S_x^{2-} (x = 4–6). When charged to 2.8 V, the peak of S_8 emerges again, which is in good accordance with the electrochemical reaction from S_8 to Li_2S and then conversion back to S_8 in a traditional Li–S battery system [48].

To further investigate this process from the perspective of structural change, in situ XRD was conducted as shown in Figure 6d,e. The sharp characteristic peaks of α-S_8 can be clearly observed at the beginning of the reaction. The peaks appear at around 27.69°, 28.64° and 31.36°, corresponding to (040), (313) and (044) of crystalline sulfur. With further lithiation, these peaks of α-S_8 gradually disappear and a new broad peak at around 27.0° appears. The peak arises due to the dissolution of crystalline sulfur and the formation of cubic Li_2S. During the charging process, Li_2S is gradually converted into a β-S_8 phase

under several steps. It is noted that the above results suggest the incomplete conversion from sulfur to Li_2S and the recrystallization of sulfur by in situ XRD [49].

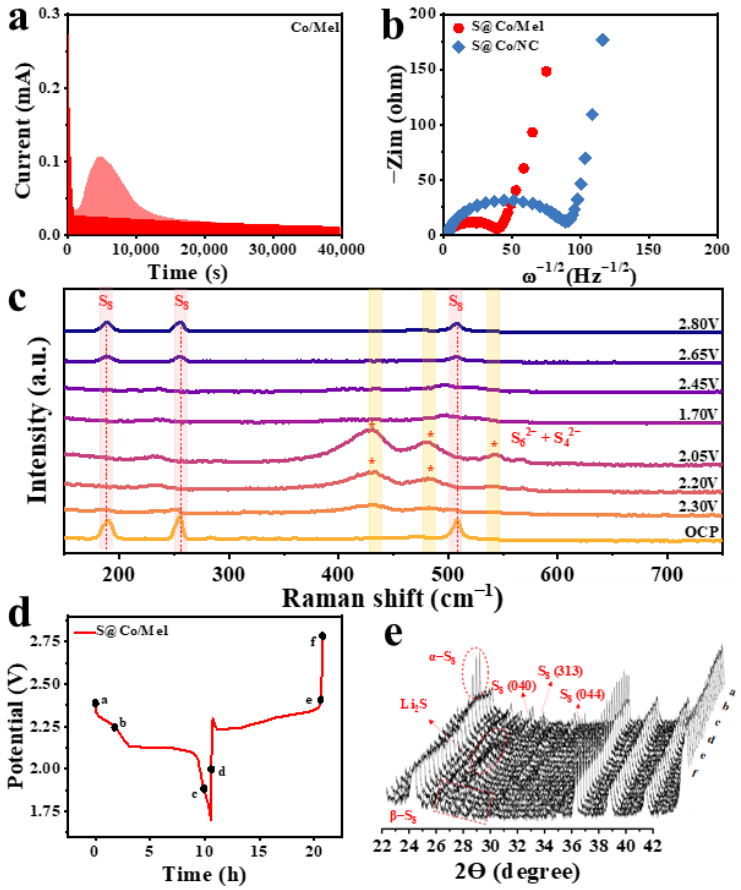

Figure 6. Potentiostatic discharge curve of the Li_2S deposition tests using Co/Mel as substrates (**a**); EIS plot (**b**); in situ Raman spectra of S@Co/Mel (**c**); charge/discharge curve obtained during in situ XRD (**d**); in situ XRD patterns during the first cycle (**e**).

Consequently, unique materials with large specific surface area and high electrical conductivity are obtained by calcining melamine and ZIF-67 during high-temperature treatment, and the rich N atoms and embedded Co NPs can accelerate polysulfide transformation in the electrochemical process. Therefore, the S@Co/Mel electrode plays a vital role in limiting the shuttle effect by simultaneously acting as a chemical catalyst as well as a polysulfide trap.

4. Conclusions

In summary, the characterization of the crystal structure and morphology illustrates the advantageous features of the S@Co/Mel composite synthesized in situ by one-step melamine-sacrificed pyrolysis: (1) a hierarchical structure with abundant mesopores capable of anchoring massive amount of sulfur, leading to extended cyclability; (2) metal nanoparticles doped in the carbon matrix with strong chemical restraint and strong interaction with sulfur species to facilitate lithium polysulfide adsorption and ionic/electronic transportation; (3) an interconnected conductive network grown in situ on the ZIF-67 surface which can further achieve an overall high conductivity to improve sulfur utilization and initial coulombic efficiency. All these merits ensure the outstanding electrochemical performance of S@Co/Mel in Li-S batteries. The long-term cycling stability of S@Co/Mel is promising as it retains a high capacity of 563 mAh g^{-1} after 1000 cycles, with a low decay rate of 0.028% per cycle. More importantly, in situ Raman and in situ XRD demonstrate the

electrocatalytic mechanism, which provides good insights for the elaborate design of more efficient electrocatalysts for high-performance Li-S batteries.

Supplementary Materials: The following supporting information can be downloaded at: https://www.mdpi.com/article/10.3390/batteries8100161/s1, Figure S1: FESEM image and the corresponding EDS mapping of Co/Mel; Figure S2: XRD spectra of ZIF-67 (a); Co/NC and S@Co/NC (b); Raman spectra of S (c); Co/NC and S@Co/NC (d); Figure S3: N_2 adsorption/desorption isotherm and pore size distribution curve of S@Co/Mel (a,b); N_2 adsorption/desorption isotherm and pore size distribution curve of Co/NC (c,d); Figure S4: CV curves of S@Co/NC for three initial cycles at the scan rate of 0.1 mV s^{-1} (a); corresponding charge/discharge curve at 0.1 C (b); specific capacity at different C rates (c); cycling performance at 0.5 C (d); Figure S5: Polysulfide adsorption experiment and UV–vis adsorption spectra of Li_2S_6 solution before and after adding Co/Mel and Co/NC; Figure S6: the CV curves of the cells with S@Co/Mel and S@Co/NC; Table S1. The comparison of cathode materials for Li-S batteries [50–56].

Author Contributions: Conceptualization, methodology, data curation, writing—original draft, H.W.; material preparation, S.J.; theoretical support, W.T.; physical Characterization, J.Z.; physical Characterization, H.L.; writing—review and editing, S.B.; supervision, Y.L.; funding acquisition, M.X. All authors have read and agreed to the published version of the manuscript.

Funding: This research was funded by the National Natural Science Foundation of China, grant number 22179190.

Data Availability Statement: The data presented in this study are available on request from the corresponding author.

Acknowledgments: We would like to thank the National Natural Science Foundation of China and the Faculty of Materials and Energy.

Conflicts of Interest: The authors declare no conflict of interest.

References

1. Mauger, A.; Julien, C.M.; Armand, M.; Zaghib, K. Tribute to john b. Goodenough: From magnetism to rechargeable batteries. *Adv. Energy Mater.* **2021**, *11*, 2000773. [CrossRef]
2. Chen, Y.; Wang, T.; Tian, H.; Su, D.; Zhang, Q.; Wang, G. Advances in lithium-sulfur batteries: From academic research to commercial viability. *Adv. Mater.* **2021**, *33*, 2003666. [CrossRef] [PubMed]
3. Xiong, X.; Yan, W.; Zhu, Y.; Liu, L.; Fu, L.; Chen, Y.; Yu, N.; Wu, Y.; Wang, B.; Xiao, R. $Li_4Ti_5O_{12}$ coating on copper foil as ion redistributor layer for stable lithium metal anode. *Adv. Energy Mater.* **2022**, *12*, 2103112. [CrossRef]
4. Zhou, Q.; Yang, X.; Xiong, X.; Zhang, Q.; Peng, B.; Chen, Y.; Wang, Z.; Fu, L.; Wu, Y. A solid electrolyte based on electrochemical active $Li_4Ti_5O_{12}$ with pvdf for solid state lithium metal battery. *Adv. Energy Mater.* **2022**, *12*, 2201991. [CrossRef]
5. Ji, X.; Lee, K.T.; Nazar, L.F. A highly ordered nanostructured carbon-sulphur cathode for lithium-sulphur batteries. *Nat. Mater.* **2009**, *8*, 500–506. [CrossRef] [PubMed]
6. Castillo, J.; Qiao, L.; Santiago, A.; Judez, X.; de Buruaga, A.S.; Jimenez, G.; Armand, M.; Zhang, H.; Li, C. Perspective of polymer-based solid-state li-s batteries. *Energy Mater.* **2022**, *2*, 200003. [CrossRef]
7. Ruan, J.; Sun, H.; Song, Y.; Pang, Y.; Yang, J.; Sun, D.; Zheng, S. Constructing 1D/2D interwoven carbonous matrix to enable high-efficiency sulfur immobilization in li-s battery. *Energy Mater.* **2022**, *1*, 100018. [CrossRef]
8. Wu, W.; Pu, J.; Wang, J.; Shen, Z.; Tang, H.; Deng, Z.; Tao, X.; Pan, F.; Zhang, H. Biomimetic bipolar microcapsules derived fromstaphylococcus aureus for enhanced properties of lithium-sulfur battery cathodes. *Adv. Energy Mater.* **2018**, *8*, 1702373. [CrossRef]
9. Yu, B.; Jung, J.; Park, K.; Goodenough, J.B. A new approach for recycling waste rubber products in Li-S batteries. *Energy Environ. Sci.* **2017**, *10*, 86–90. [CrossRef]
10. Liu, X.; Huang, J.; Zhang, Q.; Mai, L. Nanostructured metal oxides and sulfides for lithium-sulfur batteries. *Adv. Mater.* **2017**, *29*, 1601759. [CrossRef] [PubMed]
11. Bonnick, P.; Muldoon, J. The dr jekyll and mr hyde of lithium sulfur batteries. *Energy Environ. Sci.* **2020**, *13*, 4808–4833. [CrossRef]
12. Liu, H.; Yu, H. Ionic liquids for electrochemical energy storage devices applications. *J. Mater. Sci. Technol.* **2019**, *35*, 674–686. [CrossRef]
13. Geng, P.; Du, M.; Wu, C.; Luo, T.; Zhang, Y.; Pang, H. Ppy-constructed core-shell structures from mofs for confining lithium polysulfides. *Inorg. Chem. Front.* **2022**, *9*, 2389–2394. [CrossRef]
14. Furukawa, H.; Cordova, K.E.; O Keeffe, M.; Yaghi, O.M. The chemistry and applications of metal-organic frameworks. *Science* **2013**, *341*, 1230444. [CrossRef] [PubMed]

15. Qi, F.; Sun, Z.; Fan, X.; Wang, Z.; Shi, Y.; Hu, G.; Li, F. Tunable interaction between metal-organic frameworks and electroactive components in lithium-sulfur batteries: Status and perspectives. *Adv. Energy Mater.* **2021**, *11*, 2100387. [CrossRef]
16. Talin, A.A.; Centrone, A.; Ford, A.C.; Foster, M.E.; Stavila, V.; Haney, P.; Kinney, R.A.; Szalai, V.; El Gabaly, F.; Yoon, H.P.; et al. Tunable electrical conductivity in metal-organic framework thin-film devices. *Science* **2014**, *343*, 66–69. [CrossRef] [PubMed]
17. Hendon, C.H.; Rieth, A.J.; Korzyński, M.D.; Dincă, M. Grand challenges and future opportunities for metal-organic frameworks. *ACS Cent. Sci.* **2017**, *3*, 554–563. [CrossRef] [PubMed]
18. Stavila, V.; Talin, A.A.; Allendorf, M.D. Mof-based electronic and opto-electronic devices. *Chem. Soc. Rev.* **2014**, *43*, 5994–6010. [CrossRef]
19. Yang, M.; Jiao, L.; Dong, H.; Zhou, L.; Teng, C.; Yan, D.; Ye, T.; Chen, X.; Liu, Y.; Jiang, H. Conversion of bimetallic mof to ru-doped cu electrocatalysts for efficient hydrogen evolution in alkaline media. *Sci. Bull.* **2021**, *66*, 257–264. [CrossRef]
20. Downes, C.A.; Marinescu, S.C. Electrocatalytic metal-organic frameworks for energy applications. *Chemsuschem* **2017**, *10*, 4374–4392. [CrossRef]
21. Zhao, M.; Lu, Q.; Ma, Q.; Zhang, H. Two-dimensional metal-organic framework nanosheets. *Small Methods* **2017**, *1*, 1600030. [CrossRef]
22. Wang, F.; Feng, T.; Jin, X.; Zhou, Y.; Xu, Y.; Gao, Y.; Li, H.; Lei, J. Atomic co/ni active sites assisted mof-derived rich nitrogen-doped carbon hollow nanocages for enhanced lithium storage. *Chem. Eng. J.* **2021**, *420*, 127583. [CrossRef]
23. He, J.; Chen, Y.; Lv, W.; Wen, K.; Xu, C.; Zhang, W.; Li, Y.; Qin, W.; He, W. From metal–organic framework to Li_2S@C-Co-N nanoporous architecture: A high-capacity cathode for lithium-sulfur batteries. *ACS Nano* **2016**, *10*, 10981–10987. [CrossRef] [PubMed]
24. Bai, S.; Liu, X.; Zhu, K.; Wu, S.; Zhou, H. Metal-organic framework-based separator for lithium-sulfur batteries. *Nat. Energy* **2016**, *1*, 1–6. [CrossRef]
25. Zhang, H.; Xin, S.; Li, J.; Cui, H.; Liu, Y.; Yang, Y.; Wang, M. Synergistic regulation of polysulfides immobilization and conversion by mof-derived cop-hnc nanocages for high-performance lithium-sulfur batteries. *Nano Energy* **2021**, *85*, 106011. [CrossRef]
26. Jeon, Y.; Lee, J.; Jo, H.; Hong, H.; Lee, L.Y.S.; Piao, Y. Co/Co_3O_4-embedded n-doped hollow carbon composite derived from a bimetallic mof/zno core-shell template as a sulfur host for li-s batteries. *Chem. Eng. J.* **2021**, *407*, 126967. [CrossRef]
27. Xie, Y.; Cao, J.; Wang, X.; Li, W.; Deng, L.; Ma, S.; Zhang, H.; Guan, C.; Huang, W. MOF-derived bifunctional $Co_{0.85}Se$ nanoparticles embedded in n-doped carbon nanosheet arrays as efficient sulfur hosts for lithium-sulfur batteries. *Nano Lett.* **2021**, *21*, 8579–8586. [CrossRef]
28. Chen, M.; Zhao, G.; Shao, L.; Yuan, Z.; Jing, Q.; Huang, K.; Huang, Z.; Zhao, X.; Zou, G. Controlled synthesis of nickel encapsulated into nitrogen-doped carbon nanotubes with covalent bonded interfaces: The structural and electronic modulation strategy for an efficient electrocatalyst in dye-sensitized solar cells. *Chem. Mater.* **2017**, *29*, 9680–9694. [CrossRef]
29. Wu, A.; Liu, D.; Tong, L.; Yu, L.; Yang, H. Magnetic properties of nanocrystalline Fe/Fe_3C composites. *Crystengcomm* **2011**, *13*, 876–882. [CrossRef]
30. Xu, H.; Zhao, L.; Liu, X.; Huang, Q.; Wang, Y.; Hou, C.; Hou, Y.; Wang, J.; Dang, F.; Zhang, J. Metal-organic-framework derived core-shell n-doped carbon nanocages embedded with cobalt nanoparticles as high-performance anode materials for lithium-ion batteries. *Adv. Funct. Mater.* **2020**, *30*, 2006188. [CrossRef]
31. Liu, H.; Wu, Y.; Liu, P.; Wang, H.; Xu, M.; Bao, S. Anthozoan-like porous nanocages with nano-cobalt-armed cnt multifunctional layers as a cathode material for highly stable na-s batteries. *Inorg. Chem. Front.* **2022**, *9*, 645–651. [CrossRef]
32. Chen, J.; Yuan, R.; Feng, J.; Zhang, Q.; Huang, J.; Fu, G.; Zheng, M.; Ren, B.; Dong, Q. Conductive lewis base matrix to recover the missing link of li_2S_8 during the sulfur redox cycle in Li-S battery. *Chem. Mater.* **2015**, *27*, 2048–2055. [CrossRef]
33. Yang, J.; Zhang, F.; Lu, H.; Hong, X.; Jiang, H.; Wu, Y.; Li, Y. Hollow zn/co zif particles derived from core-shell zif-67@zif-8 as selective catalyst for the semi-hydrogenation of acetylene. *Angew. Chem. Int. Ed.* **2015**, *54*, 10889–10893. [CrossRef]
34. Hu, L.; Lu, Y.; Zhang, T.; Huang, T.; Zhu, Y.; Qian, Y. Ultramicroporous carbon through an activation-free approach for li-s and na-s batteries in carbonate-based electrolyte. *ACS Appl. Mater. Inter.* **2017**, *9*, 13813–13818. [CrossRef] [PubMed]
35. Vizintin, A.; Chabanne, L.; Tchernychova, E.; Arčon, I.; Stievano, L.; Aquilanti, G.; Antonietti, M.; Fellinger, T.; Dominko, R. The mechanism of li2s activation in lithium-sulfur batteries: Can we avoid the polysulfide formation? *J. Power Sources* **2017**, *344*, 208–217. [CrossRef]
36. Xia, B.Y.; Yan, Y.; Li, N.; Wu, H.B.; Lou, X.W.; Wang, X. A metal-organic framework-derived bifunctional oxygen electrocatalyst. *Nat. Energy* **2016**, *1*, 15006. [CrossRef]
37. Tian, H.; Tian, H.; Wang, S.; Chen, S.; Zhang, F.; Song, L.; Liu, H.; Liu, J.; Wang, G. High-power lithium-selenium batteries enabled by atomic cobalt electrocatalyst in hollow carbon cathode. *Nat. Commun.* **2020**, *11*, 5025. [CrossRef]
38. Du, Z.; Chen, X.; Hu, W.; Chuang, C.; Xie, S.; Hu, A.; Yan, W.; Kong, X.; Wu, X.; Ji, H.; et al. Cobalt in nitrogen-doped graphene as single-atom catalyst for high-sulfur content lithium-sulfur batteries. *J. Am. Chem. Soc.* **2019**, *141*, 3977–3985. [CrossRef]
39. Garapati, M.S.; Sundara, R. Enhancing polysulfide confinement and redox kinetics by electrocatalytic interlayer for highly stable lithium-sulfur batteries. *Electrochim. Acta* **2020**, *362*, 137035. [CrossRef]
40. Zhou, T.; Du, Y.; Yin, S.; Tian, X.; Yang, H.; Wang, X.; Liu, B.; Zheng, H.; Qiao, S.; Xu, R. Nitrogen-doped cobalt phosphate@nanocarbon hybrids for efficient electrocatalytic oxygen reduction. *Energy Environ. Sci.* **2016**, *9*, 2563–2570. [CrossRef]

41. Hu, Q.; Wang, B.; Chang, S.; Yang, C.; Hu, Y.; Cao, S.; Lu, J.; Zhang, L.; Ye, H. Effects of annealing temperature on electrochemical performance of snsx embedded in hierarchical porous carbon with n-carbon coating by in-situ structural phase transformation as anodes for lithium ion batteries. *J. Mater. Sci. Technol.* **2021**, *84*, 191–199. [CrossRef]
42. Hu, L.; Dai, C.; Lim, J.M.; Chen, Y.; Lian, X.; Wang, M.; Li, Y.; Xiao, P.; Henkelman, G.; Xu, M. A highly efficient double-hierarchical sulfur host for advanced lithium-sulfur batteries. *Chem. Sci.* **2018**, *9*, 666–675. [CrossRef] [PubMed]
43. Dai, C.; Lim, J.; Wang, M.; Hu, L.; Chen, Y.; Chen, Z.; Chen, H.; Bao, S.; Shen, B.; Li, Y.; et al. Honeycomb-like spherical cathode host constructed from hollow metallic and polar Co_9S_8 tubules for advanced lithium-sulfur batteries. *Adv. Funct. Mater.* **2018**, *28*, 1704443. [CrossRef]
44. Ma, H.; Liu, X.; Liu, N.; Zhao, Y.; Zhang, Y.; Bakenov, Z.; Wang, X. Defect-rich porous tubular graphitic carbon nitride with strong adsorption towards lithium polysulfides for high-performance lithium-sulfur batteries. *J. Mater. Sci. Technol.* **2022**, *115*, 140–147. [CrossRef]
45. Guo, B.; Bandaru, S.; Dai, C.; Chen, H.; Zhang, Y.; Xu, Q.; Bao, S.; Chen, M.; Xu, M. Self-supported $FeCoS_4$ nanotube arrays as binder-free cathodes for lithium-sulfur batteries. *ACS Appl. Mater. Inter.* **2018**, *10*, 43707–43715. [CrossRef]
46. Li, Q.; Li, L.; Wu, P.; Xu, N.; Wang, L.; Li, M.; Dai, A.; Amine, K.; Mai, L.; Lu, J. Silica restricting the sulfur volatilization of nickel sulfide for high-performance lithium-ion batteries. *Adv. Energy Mater.* **2019**, *9*, 1901153. [CrossRef]
47. Cheng, R.; Guan, Y.; Luo, Y.; Zhang, C.; Xia, Y.; Wei, S.; Zhao, M.; Lin, Q.; Li, H.; Zheng, S.; et al. Guanine-assisted n-doped ordered mesoporous carbons as efficient capacity decaying suppression materials for lithium-sulfur batteries. *J. Mater. Sci. Technol.* **2022**, *101*, 155–164. [CrossRef]
48. Zhao, J.; Qi, Y.; Yang, Q.; Huang, T.; Wang, H.; Wang, Y.; Niu, Y.; Liu, Y.; Bao, S.; Xu, M. Chessboard structured electrode design for li-s batteries based on mxene nanosheets. *Chem. Eng. J.* **2022**, *429*, 131997. [CrossRef]
49. Zech, C.; Hönicke, P.; Kayser, Y.; Risse, S.; Grätz, O.; Stamm, M.; Beckhoff, B. Polysulfide driven degradation in lithium-sulfur batteries during cycling—Quantitative and high time-resolution operando x-ray absorption study for dissolved polysulfides probed at both electrode sides. *J. Mater. Chem. A* **2021**, *9*, 10231–10239. [CrossRef]
50. Gong, Z.; Wu, Q.; Wang, F.; Li, X.; Fan, X.; Yang, H.; Luo, Z. A hierarchical micro/mesoporous carbon fiber/sulfur composite for high-performance lithium-sulfur batteries. *Rsc Adv.* **2016**, *6*, 37443–37451. [CrossRef]
51. Peng, H.; Hou, T.; Zhang, Q.; Huang, J.; Cheng, X.; Guo, M.; Yuan, Z.; He, L.; Wei, F. Strongly coupled interfaces between a heterogeneous carbon host and a sulfur-containing guest for highly stable lithium-sulfur batteries: Mechanistic insight into capacity degradation. *Adv. Mater. Interfaces* **2014**, *1*, 1400227. [CrossRef]
52. Mao, Y.; Li, G.; Guo, Y.; Li, Z.; Liang, C.; Peng, X.; Lin, Z. Foldable interpenetrated metal-organic frameworks/carbon nanotubes thin film for lithium–sulfur batteries. *Nat. Commun.* **2017**, *8*, 14628. [CrossRef] [PubMed]
53. Yan, Y.; Li, H.; Cheng, C.; Yan, T.; Gao, W.; Mao, J.; Dai, K.; Zhang, L. Boosting polysulfide redox conversion of li-s batteries by one-step-synthesized co-mo bimetallic nitride. *J. Energy Chem.* **2021**, *61*, 336–346. [CrossRef]
54. Liu, B.; Fan, K.; Li, J.; Liu, G.; Liu, Y.; Yang, C.; Tong, H.; Han, K.; Qian, D. Carbon nanotubes-intercalated co-n-c as a robust sulfur host for lithium-sulfur batteries. *Mater. Res. Bull.* **2020**, *121*, 110625. [CrossRef]
55. Yu, H.; Zhang, B.; Sun, F.; Jiang, G.; Zheng, N.; Xu, C.; Li, Y. Core-shell polyhedrons of carbon nanotubes-grafted graphitic carbon@nitrogen doped carbon as efficient sulfur immobilizers for lithium-sulfur batteries. *Appl. Surf. Sci.* **2018**, *450*, 364–371. [CrossRef]
56. Yu, F.; Zhou, H.; Shen, Q. Modification of cobalt-containing mof-derived mesoporous carbon as an effective sulfur-loading host for rechargeable lithium-sulfur batteries. *J. Alloy. Compd.* **2019**, *772*, 843–851. [CrossRef]